Modeling of heating and cooling behaviors of laminated glass facades exposed to fire with three-dimensional flexibilities

D.A. Abdoh[b,c], Yang Zhang[a,*], A.S. Ademiloye[d], V.K.R. Kodur[e], K.M. Liew[b,c,*]

[a] School of Science, Nanjing University of Science and Technology, Nanjing 210094, China

[b] Department of Architecture and Civil Engineering, City University of Hong Kong, Kowloon, Hong Kong, China

[c] Centre for Nature-Inspired Engineering, City University of Hong Kong, Kowloon, Hong Kong, China

[d] Zienkiewicz Institute for Modelling, Data and AI, Faculty of Science and Engineering, Swansea University, Bay Campus, Swansea SA1 8EN, United Kingdom

[e] Department of Civil and Environmental Engineering, Michigan State University, East Lansing, Michigan 48824-1226, USA

Abstract

To develop a precise and efficient computer model for predicting the heating and cooling behaviors of laminated glass facades exposed to fire, there is an urgent need to reduce the huge computational requirements associated with simulating heat transfer in layered structures that feature a down-flowing water film. We overcome this challenge by proposing, for the first time, an efficient three-dimensional finite difference method (3DFDM), which has high numerical stability when solving the heat transfer equations with water film and air convection. To capture the moving particles of the water film, we developed a unique computational algorithm for particle labelling, which has two significant advantages: (1) it eliminates the time-consuming process of searching for neighboring particles in conventional meshfree methods, and (2) it ensures that every main particle interacts only with limited neighboring particles without utilizing any weights, thus significantly reducing the computational effort. We validated our proposed 3DFDM through experiments in heating and cooling scenarios and compared its thermal results with those obtained from the commercial software packages to demonstrate its high efficiency and accuracy. Furthermore, we examined the feasibility of our model in evaluating the effects of thickness of the interlayer (PVB layer) and water film release time on the cooling behavior of laminated glass during a fire.

Keywords: Three-dimensional finite difference method (3DFDM); Laminated glass facades; Down-flowing water; Heating and cooling behaviors; Thermal response; Fire

* Corresponding authors

E-mail addresses: hfutzy@njust.edu.cn (Yang Zhang); kmliew@cityu.edu.hk (K.M. Liew)

1. Introduction

In recent years, there has been a significant increase in the number of studies aimed at understanding the mechanisms underlying laminated glass protection during a fire. When glass facades are broken during a fire, more fresh air enters the structure, causing fire flashover which often leads to catastrophic consequences [1]. To prevent this, an effective protective facility, water sprays, is used in fire suppression [2]. Glass facades can be protected from failure if the cooling by water sprays is properly understood and controlled [3]. Various kinds of experimental setups have been adopted by researchers to study the heat transfer and breakage processes of different types of glass [4,5] under various conditions [6,7] during a fire event. However, full-scale experiments are cost-intensive and require many precautions, particularly for the measurements of water film parameters during a fire incident. Therefore, there is an urgent demand for the development of an efficient and effective computational framework to simulate and predict the heating and cooling behaviors of glass facades.

Several mesh-based numerical methods have been presented to study the heat transfer mechanisms in solids. The finite element method (FEM) has been extensively employed to investigate heat transfer problems [8-10]. The finite volume method (FVM) has also been employed to study the conjugate heat transfer problems [11]. However, these mesh-based methods require huge computational effort. Moreover, the computational complexity and convergence issues of FEM [12,13] and FVM [14,15] may limit their applications in a large scale and even in more complicated boundary condition problems, particularly when the two methods (FEM and FVM) are coupled in one model [16-18]. Commercial software packages such as ANSYS [19,20], COMSOL [21,22], and Autodesk CFD [23,24] have been utilized to solve thermal transfer problems based on FVM or FEM. However, their usage is limited by accuracy and stability concerns, particularly when it comes to cooling laminated glasses during a fire, due to complex modeling system associated with moving water film particles. Besides, modeling the heating and cooling behaviors of laminated glass facades require a numerical framework that can deal with the issue of thermal redistribution caused by heat exchange between the water film and laminated glass, and the strong nonlinearity of the system under differential thermal stresses. This presents a formidable challenge for FEM-based methods.

Apart from mesh-based numerical methods, meshfree methods [25-29] such as smoothed particle hydrodynamics (SPH) have been utilized to simulate heat transfer in incompressible flows [30,31] and the motion of cooling lubricant in drilling processes [32]. Glass cooling has also been simulated when exposed to heat radiation using the SPH method [33,34] and the finite point method [35]. More recently, a machine learning-based approach was proposed for solving partial differential equations (PDEs) [36] such as the heat transfer equation. This involves building the deep neural networks (DNNs) and training them by minimizing the loss function. Despite the attractiveness of the previous methods, several computational challenges need to be investigated and resolved. For instance, the optimization process may add more complexity to the research problem and in some cases, a linear problem may be converted to a nonlinear one [36].

The generalized finite difference method (GFDM) was recently proposed [37-39] to solve the PDEs. The GFDM is mainly devoted to unstructured or irregular grids, where every main particle is interacting with neighboring particles (a star of the main particle) in a specific control scheme according to the weighting function. The near particles have a greater effect on the main particles than the far neighboring particles. Accordingly, the number and arrangement of node stars have a significant effect on the model stability and accuracy (e.g., 9-nodes stars may lead to an ill-conditioned system [38]). Therefore, a greater number of node stars must be considered to achieve a well-conditioned system. Moreover, the GFDM may not be suitable for modelling of the heating and cooling behaviors of laminated glass due to the following reasons: (1) it requires a huge computational cost since the thermal interaction during the cooling stage occurs between the water film and glass, therefore, the searching process of neighboring particles needs to be conducted at each time step as the water particles are moving, (2) since each of the fixed glass particle needs to interact with many neighboring particles, the associated computational cost may grow significantly with a slight increase in the number of neighboring particles, and (3) the stability of GFDM is also governed by the weight function, and simulating heat transfer in different materials and moving fluid using the existing weight function may not be sufficient.

To overcome the abovementioned limitation in the GFDM, we propose a new three-dimensional finite difference method (3DFDM) to simulate the heating and cooling behaviors

of laminated glass. In our 3DFDM, we use only the Taylor series expansion to approximate the second derivatives of the heat transfer equation, without a weight function or mesh. The number of neighboring particles will be limited to six in three-dimensional (3D) space with two particles in each direction. Despite the large number of particles and small time steps used in our algorithm, the labeling strategy adopted, particularly with the down-flowing water film particles, enables an efficient thermal simulation in the laminated glass. The proposed 3DFDM have several advantages over existing numerical methods in terms of efficiency and stability, and it is easy to implement. The 3DFDM is not intended to be used in this study to solve the uncertainties in the input parameters and their effects on the thermal outputs in contrast with the machine learning approach [36]. The MATLAB sensitivity analysis toolbox [40] may be used to quantify the influence of uncertain input parameters on the thermal results. The effects of Polyvinyl butyral (PVB) thickness and water film release time, however, are investigated in this study to provide the outlines for optimum thermal design of laminated glass in improving the fire safety. The 3DFDM can be extended to study thermal fractures in composites materials and structures [41-43].

The remainder of this paper are structured as follows. Section 2 presents the theoretical formulations for the heat transfer equation, 3DFDM and the heat transfer mechanism in laminated glass. Section 3 illustrates the computational details of our 3DFDM, including the highly efficient algorithm. Section 4 presents the results, including the validation and the effects of PVB thickness and water film release time (WFRT) on the thermal behavior of laminated glass. Finally, the conclusions from this study are summarized in Section 5.

2. Theoretical formulation

2.1. Heat transfer equation

The main differential equation used in this study is the heat transfer equation [20,21,33] in 3D as shown in Eq. (1)

$$\frac{\partial T}{\partial t} = \frac{k}{\rho C_p} \nabla^2 T + \frac{q}{\rho c_p}, \quad (1)$$

$$\nabla^2 T = \frac{\partial^2 T}{\partial x^2} + \frac{\partial^2 T}{\partial y^2} + \frac{\partial^2 T}{\partial z^2}, \quad (2)$$

where T is the temperature, t is the current time, $\nabla^2 T$ represents the Laplacian of temperature in the x-, y-, and z-directions as shown in Eq. (2), k is the thermal conductivity, ρ is the material density, C_p is the specific heat capacity, and q is the heat flux. Thermal conduction within the domain or convection with the external surrounding environment is simulated when q value is substituted with zero (Eq. (3)) or $h\,(T - T_\infty)$ (Eq. (4)) [44], respectively, where T_∞ is the temperature of the external surrounding environment like air and h is the heat transfer coefficient:

$$\frac{\partial T}{\partial t} = \frac{k}{\rho C_p} \nabla^2 T, \quad (3)$$

$$\frac{\partial T}{\partial t} = \frac{k}{\rho C_p} \nabla^2 T + \frac{h\,(T - T_\infty)}{\rho C_p}, \quad (4)$$

2.2. Computational procedure

According to the 3DFDM model, the domain is discretized into a finite number of particles without using any mesh in contrast to the conventional FDM. Moreover, variables, such as temperature, are solved based on the particle's location and not to the fixed location of the node. In this way, the thermal interaction between moving fluid (water) and fixed solid (glass) is adequately represented, thereby avoiding mesh distortion. As a major departure from GFDM, every main particle interacts only with six neighboring particles without the use of any weight function. Furthermore, compared to GFDM which requires a costly searching process for neighboring particles at every time step, our 3DFDM is more efficient due to the novel algorithm adopted.

In our 3DFDM, the first temporal derivative of temperature $\left(\frac{\partial T}{\partial t}\right)$ is replaced with FDM

approximation of the first derivative according to the forward difference scheme as shown in Eq. (5). In which, T is estimated at particle location x, y, z. Second derivatives of temperature in three directions are replaced with FDM approximations at central difference scheme (applied for most particles) as shown in Eqs. (6) to (8). Note that $T_{x,y,z}$ refers to the temperature value at time t.

$$\frac{\partial T}{\partial t}_{FDM-F} = \frac{T_{x,y,z(t+\Delta t)} - T_{x,y,z}}{\Delta t}, \tag{5}$$

$$\frac{\partial^2 T}{\partial x^2}_{FDM-C} = \frac{T_{x-\Delta x,y,z} - 2T_{x,y,z} + T_{x+\Delta x,y,z}}{\Delta x^2}, \tag{6}$$

$$\frac{\partial^2 T}{\partial y^2}_{FDM-C} = \frac{T_{x,y-\Delta y,z} - 2T_{x,y,z} + T_{x,y+\Delta y,z}}{\Delta y^2}, \tag{7}$$

$$\frac{\partial^2 T}{\partial z^2}_{FDM-C} = \frac{T_{x,y,z-\Delta z} - 2T_{x,y,z} + T_{x,y,z+\Delta z}}{\Delta z^2}, \tag{8}$$

where Δt is the time step, Δx, Δy, and Δz are the differences in distances between particles in the x-, y-, and z-directions, respectively. Note that Δx, Δy, and Δz are equal to spacings between particles in the x-, y-, and z-directions, respectively, as shown in Fig. 1. $T_{x,y,z}$ and $T_{x,y,z(t+\Delta t)}$ are the temperature of the main particle at coordinate locations x, y, and z at the current and next time steps, respectively. $T_{x-\Delta x,y,z}$, $T_{x+\Delta x,y,z}$, $T_{x,y-\Delta y,z}$, $T_{x,y+\Delta y,z}$, $T_{x,y,z+\Delta z}$ and $T_{x,y,z-\Delta z}$ are the temperature of nearby particles as shown in Fig. 1, where each main particle interacts with only two adjacent particles in each direction (six particles for the x-, y-, and z-directions).

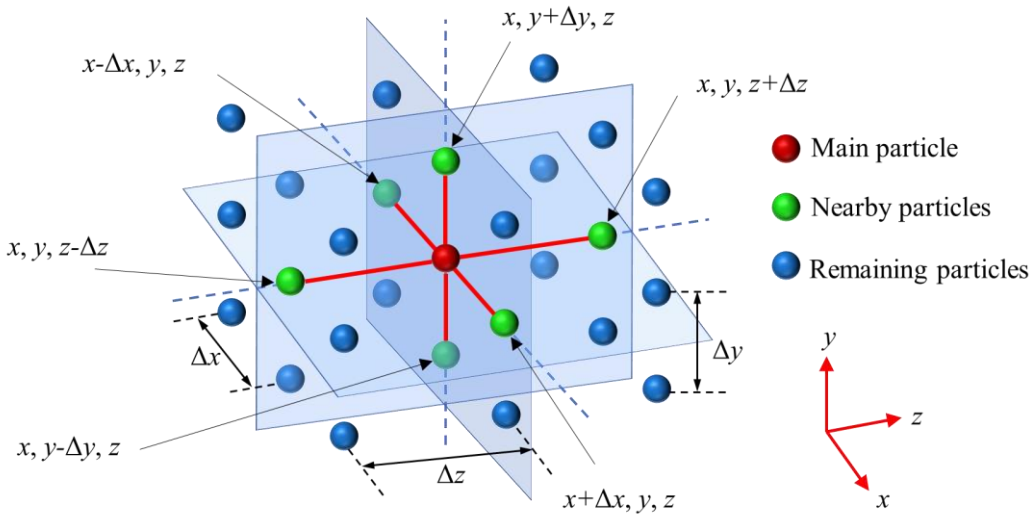

Fig. 1. Illustrative diagram showing particle locations and spacings in the *x*-, *y*-, and *z*-directions according to central difference approximation, where the main particle is located at *x*, *y* and *z*.

The forward difference and backward difference schemes for Eq. (8) are illustrated in Eqs. (9) and (10), respectively, if the main direction of heat transfer is in the *z*-direction. The subscripts *F*, *C*, and *B* refer to forward difference, central difference and backward difference schemes, respectively.

$$\left(\frac{\partial^2 T}{\partial z^2}\right)_{FDM-F} = \frac{T_{x,y,z} - 2T_{x,y,z+\Delta z} + T_{x,y,z+2\Delta z}}{\Delta z^2}, \tag{9}$$

$$\left(\frac{\partial^2 T}{\partial z^2}\right)_{FDM-B} = \frac{T_{x,y,z} - 2T_{x,y,z-\Delta z} + T_{x,y,z-2\Delta z}}{\Delta z^2}. \tag{10}$$

Then we define $\nabla^2 T_F$, $\nabla^2 T_C$ and $\nabla^2 T_B$ as the Laplacian of temperature at *z*-direction (main heat transfer direction), which are estimated at the forward difference, central difference and backward difference schemes as depicted in Eqs. (11) to (13), respectively:

$$\nabla^2 T_F = \left(\frac{\partial^2 T}{\partial x^2}\right)_{FDM-C} + \left(\frac{\partial^2 T}{\partial y^2}\right)_{FDM-C} + \left(\frac{\partial^2 T}{\partial z^2}\right)_{FDM-F} \tag{11}$$

$$\nabla^2 T_C = \frac{\partial^2 T}{\partial x^2}_{FDM-C} + \frac{\partial^2 T}{\partial y^2}_{FDM-C} + \frac{\partial^2 T}{\partial z^2}_{FDM-C} \tag{12}$$

$$\nabla^2 T_B = \frac{\partial^2 T}{\partial x^2}_{FDM-C} + \frac{\partial^2 T}{\partial y^2}_{FDM-C} + \frac{\partial^2 T}{\partial z^2}_{FDM-B} \tag{13}$$

159 To discretize the heat transfer equation at radiation mode (z-direction), first temporal
160 derivative of temperature and $\nabla^2 T$ in Eq. (1) are replaced with Eq. (5) and $\nabla^2 T_F$, respectively,
161 as shown in Eq. (14):

$$T_{x,y,z(t+\Delta t)} = \left(\frac{k}{\rho C_p}\nabla^2 T_F + \frac{Q}{\rho C_p}\right)\Delta t + T_{x,y,z} \tag{14}$$

162 Similarly, Eq. (3) is discretized but $\nabla^2 T$ is replaced with $\nabla^2 T_C$ as shown in Eq. (15):

$$T_{x,y,z(t+\Delta t)} = \frac{k\Delta t}{\rho C_p}\nabla^2 T_C + T_{x,y,z} \tag{15}$$

163 When heat is transferred to the surrounding air by convection at the end of the domain in the
164 z-direction, $\nabla^2 T$ is replaced by $\nabla^2 T_B$ as shown in Eq. (16):

$$T_{x,y,z(t+\Delta t)} = \left(\frac{k}{\rho C_p}\nabla^2 T_B + \frac{h\,(T - T_\infty)}{\rho C_p}\right)\Delta t + T_{x,y,z} \tag{16}$$

165 *2.3. Problem definition*

166 In this study, we aim to investigate the heating and cooling cases of laminated glass under
167 the actions of fire and down-flowing water film. Therefore, different material properties (glass,
168 PVB or water) and heat transfer modes are considered in the formulation as shown in Fig. 2.

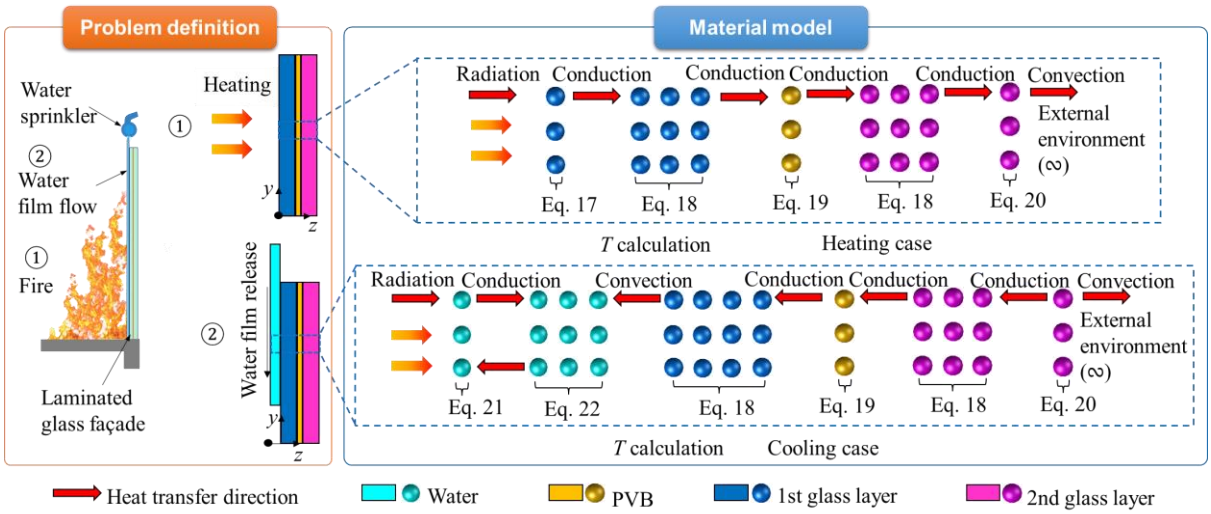

Fig. 2. Heat and cooling transfer directions and modes in laminated glass, where the temperature values of water, PVB and glass are calculated according to Eqs. (17) to (22).

First, heat is transferred from the fire source to the exposed glass particles (exposed face) by means of radiation according to Eq. (17), where k_G is the thermal conductivity of glass, ρ_G is the glass density, C_{pG} is the specific heat capacity of glass and Q is the heat flux:

$$T_{x,y,z(t+\Delta t)} = \left(\frac{k_G}{\rho_G C_{pG}}\nabla^2 T_F + \frac{Q}{\rho_G C_{pG}}\right)\Delta t + T_{x,y,z} \tag{17}$$

Then the conductive heat transfer from the exposed glass particles (exposed face) to the remaining glass particles is presented in Eq. (18):

$$T_{x,y,z(t+\Delta t)} = \frac{k_G \Delta t}{\rho_G C_{pG}}\nabla^2 T_C + T_{x,y,z} \tag{18}$$

Heat is transferred from 1st glass layer to the PVB particles by means of conduction, where it can be used to obtain the temperature of PVB particles by replacing glass material with PVB as shown in Eq. (19), where k_{PVB} is the thermal conductivity of PVB, ρ_{PVB} is the PVB density and C_{pPVB} is the specific heat capacity of PVB:

$$T_{x,y,z(t+\Delta t)} = \frac{k_{PVB}\Delta t}{\rho_{PVB}C_{pPVB}}\nabla^2 T_C + T_{x,y,z} \tag{19}$$

The temperature can also be calculated from the heat transferred from PVB particles to the 2nd glass layer and within the 2nd glass layer particles by conduction using Eq. (18).

Heat is transferred from the ambient face of 2nd glass layer to the surrounding air through convection as shown in Eq. (20) and Fig. 2:

$$T_{x,y,z(t+\Delta t)} = \left(\frac{k_G}{\rho_G C_{pG}}\nabla^2 T_B + \frac{h\,(T - T_\infty)}{\rho_G C_{pG}}\right)\Delta t + T_{x,y,z} \tag{20}$$

In the cooling process, when water film is applied at the exposed face of the 1st glass layer, heat is transferred from the fire to the exposed water film particles by means of radiation as shown in Eq. (21) and Fig. 2, where k_W is the thermal conductivity of water, ρ_W is the water density and C_{pW} is the specific heat capacity of water:

$$T_{x,y,z(t+\Delta t)} = \left(\frac{k_W}{\rho_W C_{pW}}\nabla^2 T_F + \frac{Q}{\rho_W C_{pW}}\right)\Delta t + T_{x,y,z} \tag{21}$$

Heat is transferred from the exposed water film particles to the remaining water film particles by means of conduction as shown in Eq. (22) and Fig. 2:

$$T_{x,y,z(t+\Delta t)} = \frac{k_W\Delta t}{\rho_W C_{pW}}\nabla^2 T_C + T_{x,y,z} \tag{22}$$

The cooling of the laminated glass is simulated by calculating the temperature of glass and PVB particles according to Eqs. (17) to (22) as shown in Fig. 2.

3. Computational framework

3.1. 3DFDM discretization

The details of the 3DFDM discretization employed in this study are illustrated in Fig. 3. In our model, the convection with air at the ambient surface of laminated glass and heat flux (fire) at the exposed surface of the glass are the thermal boundary conditions. Convection with air is presented by applying a convective heat transfer coefficient (h) at the back of the laminated glass. This provides a more realistic modeling of the problem, particularly if the experiment is conducted in a cold, open area [4,44]. Noted that layers are used to indicate each material or composite segment, while surfaces are used to indicate the number of divisions in z-direction at each layer.

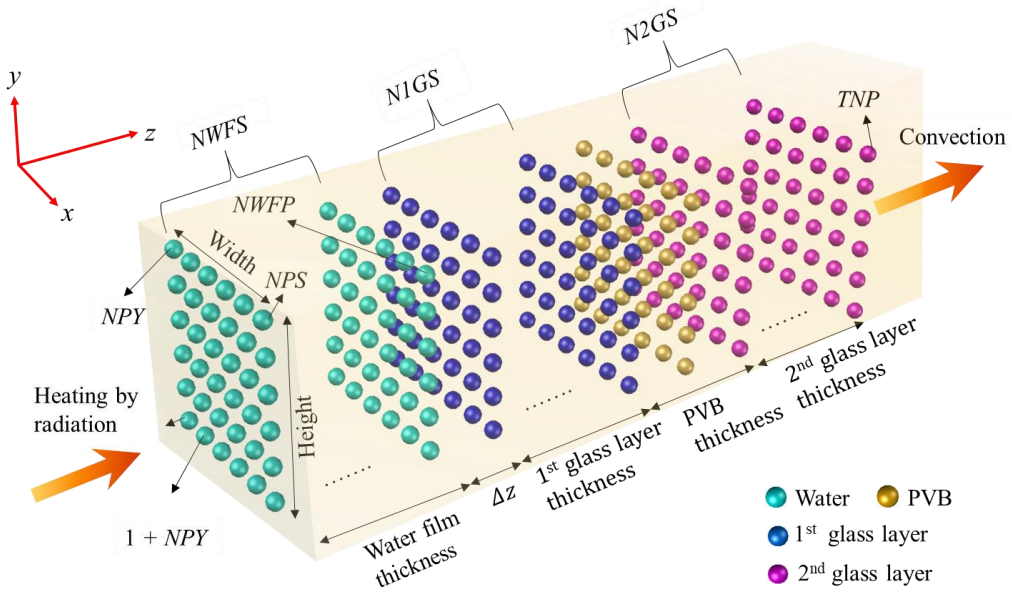

Fig. 3. The 3DFDM discretization of laminated glass and water.

Particle labeling is important to our modeling technique and algorithm. Labeling starts from the origin of the x, y, and z axes, as shown in Fig 3. First, the particles are labeled in the y-direction from the bottom ($y = 0$) until the top particle is reached (NPY), as shown in Fig. 3. In the same manner, adjacent particles are labeled in the x-direction until all surface particles are labeled (NPS represents the total particles at each surface). The other surfaces are also labeled similarly. $N1GS$ is the number of 1st glass layer surfaces and $N2GS$ is the number of 2nd glass layer surfaces. For instance, suppose we divide the water and glass layers to a total number of

surfaces equals 19 (*TNS* = 19) and each surface into 80 divisions in both the *x*- and *y*-directions: *NPS* equals 6,400 particles (80 × 80) at each surface, and the total number of particles (*TNP*) is 121,600 (6,400 × 19). Therefore, the coordinates of particle i = 1 are x = 0, y = 0, z = 0; the coordinates of particle i = 6,400 are x = 0.6 m, y = 0.6 m, z = 0; and the coordinates of particle i = 121,600 are x = 0.6 m, y = 0.6 m, z = 0.01338 m with width 0.6 m, height 0.6 m and the total thickness of laminated glass with water film of 0.01338 m. *TNP* and the number of water film particle (*NWFP*) are calculated according to Eqs. (23) and (24), respectively,

$$TNP = TNS \times NPS, \tag{23}$$

$$NWFP = NWFS \times NPS, \tag{24}$$

where *NWFS* is the number of water film surfaces. Suppose that the label of the main particle is i, the differences in label numbers of nearby particles are *NPY*, 1 and *NPS* at *x*-, *y*-, and *z*-directions, respectively, according to our labeling strategy. Therefore, the coordinate locations that appeared in the format of *x*, *y*, *z* in Eqs (5) to (10) are replaced with label numbers as shown in Eqs. (25) to (30), respectively.

$$\frac{\partial T}{\partial t}_{FDM-F} = \frac{T_{i(t+\Delta t)} - T_i}{\Delta t}, \tag{25}$$

$$\frac{\partial^2 T}{\partial x^2}_{FDM-C} = \frac{T_{i-NPY} - 2T_i + T_{i+NPY}}{\Delta x^2}, \tag{26}$$

$$\frac{\partial^2 T}{\partial y^2}_{FDM-C} = \frac{T_{i-1} - 2T_i + T_{i+1}}{\Delta y^2}, \tag{27}$$

$$\frac{\partial^2 T}{\partial z^2}_{FDM-C} = \frac{T_{i-NPS} - 2T_i + T_{i+NPS}}{\Delta z^2}, \tag{28}$$

$$\frac{\partial^2 T}{\partial z^2}_{FDM-F} = \frac{T_i - 2T_{i+NPS} + T_{i+2NPS}}{\Delta z^2}, \tag{29}$$

$$\frac{\partial^2 T}{\partial z^2}_{FDM-B} = \frac{T_i - 2T_{i-NPS} + T_{i-2NPS}}{\Delta z^2}. \tag{30}$$

It should be noted that the subscripts Δx, Δy and Δz associated with temperature (T) as shown

in Eqs. (5) to (10) are replaced with *NPY*, 1 and *NPS*, respectively, and *x*, *y*, *z* are replaced with *i* as depicted in Eqs. (25) to (30). For instance, $T_{x+\Delta x,y,z}$ or T_{i+NPY} is equivalent to the temperature of the particle with a label number equal to 1+ *NPY* if the label number of the main particle is 1 (i = 1). Similarly, $T_{x-\Delta x,y,z}$ or T_{i-NPY} is equivalent to the temperature of particle with a label number equal to *NPS* – *NPY* if the label number of the main particle is *NPS* (i = *NPS*). For main particles located at interfaces, *T* is calculated in the same manner and with the same material properties of the main particle. For example, if the label number of the main particle is *NWFP* (water), the temperature values of the nearby particles in the *z*-direction are the temperature values of particles with label numbers of *NWFP* – *NPS* (water) and *NWFP* + *NPS* (glass). Meanwhile, the temperature of main particle (i = *NWFP*) with the water properties will be calculated using Eq. (22).

Fig. 4 illustrates the water film application in our 3DFDM. When time (t) is less than water film release time (t_w), water film particles are held fixed at the top of laminated glass (y = H) as shown in Fig. 4. When water film is released at time t_w, water film particles flowing downward in the *y*-direction by a distance equals Δy for each time step (*TS*). *TS* is calculated according to Eq. (31)

$$TS = \frac{\Delta y}{V}, \tag{31}$$

where *V* is the down-flowing velocity of the water film. Note that *TS* is calculated based on Δy and *V* to ensure that each water film particle coincides exactly with the adjacent exposed glass particles. Cooling for each glass particle at the exposed surface is activated when its *y*-coordinate equals the *y*-coordinate of the first approaching water film particle. As shown in Fig. 4, when the first row of water film particles reaches the half-height of laminated glass, the exposed glass particles located at or above the mid-height of laminated glass ($y \geq 0.5\ H$) are influenced by water film, whereas the exposed glass particles located below the half-height ($y < 0.5\ H$) are not yet influenced with water film particles.

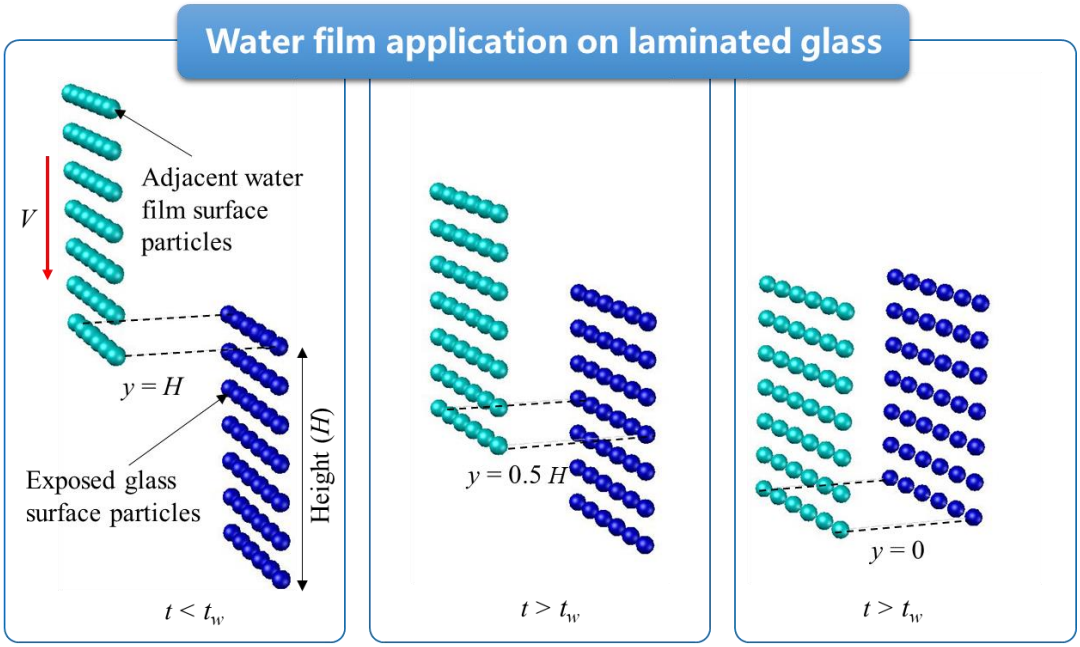

Fig. 4. Illustrative diagram showing water film application on laminated glass at different times, where t_w is the water film release time, H is the height of laminated glass and V is the down-flowing velocity of the water film.

3.2. Numerical algorithm

The detailed algorithm for our 3DFDM is presented in Table 1. The simulation time is divided into two cases: before and after the water film releases. In the heating case, the temperature calculation of exposed glass particles proceeds from label numbers $NWFP + 1$ to $NWFP + NPS$, with water film particles excluded. Similarly, in the cooling case, the exposed surface particles are those located on the first surface of the water film ($i = 1$ to NPS). When the temperature values are computed for the exposed surface particles, the temperature values for the other particles are calculated based on the convection and conduction from the exposed surface. The temperature values for all particles are saved at the end of a time step to be used in the next subsequent time steps. Notably, to minimize the computational time, loops are executed only within the required particles. For instance, water film particles are excluded from the heating case (before water film release), and exposed surface particles are separated from the other particles in both the heating and cooling cases (before and after water film release), as shown in Table 1.

Table 1. Algorithm illustrating the steps in our proposed 3DFDM

Define geometry, material properties, and thermal boundary conditions.

Calculate the *TS* according to Eq. (31).

For $k = 1$ **to** ***TNSS*** (total number of simulation steps)

  If $t < t_w$ (heating case)

    For $i = NWFP + 1$ **to** $NWFP + NPS$ (exposed glass particles)

      Calculate *T* according to Eq. (17).

    End

    For $i = NWFP + NPS + 1$ **to** ***TNP*** (for remaining glass and PVB particles)

      Calculate *T* according to Eqs. (18) to (20).

    End

  Else (cooling case)

    For $i = 1$ **to** ***NPS*** (exposed water film particles)

      Calculate *T* according to Eq. (21).

    End

    For $i = NPS + 1$ **to** ***NWFP*** (remaining water film particles)

      Calculate *T* according to Eq. (22).

    End

    For $i = NWFP + 1$ **to** ***TNP*** (glass and PVB particles)

      Calculate *T* according to Eqs. (18) to (20).

    End

  End if

End

4. Results and discussion

We programmed our 3DFDM using MATLAB software and validated it by comparing our numerical results with experimental measurements from various thermal cases and conditions. Moreover, a detailed computational comparison was conducted between our 3DFDM and Autodesk CFD to prove the high efficiency of our proposed model. All the numerical simulations were executed on an HP Laptop with an Intel® Core® i7-8550U CPU @ 1.80GHz,

1992 Mhz, 4 Core(s), 8 Logical Processor, and 8 GB of RAM. The material properties of glass, PVB and water are presented in Table 2 [4,44].

Table 2. Material properties of glass, PVB, and water [4,44].

Material	Property	Symbol	Value	Unit
Glass	Density	ρ_G	2500	Kg/m^3
	Thermal conductivity	K_G	0.94	W/m.K
	Specific heat capacity	C_{pG}	820	J/Kg.K
	Thermal diffusivity	α_G	4.585×10^{-7}	m^2/s
PVB	Density	ρ_{PVB}	1070	Kg/m^3
	Thermal conductivity	K_{PVB}	0.221	W/m.K
	Specific heat capacity	C_{pPVB}	1100	J/Kg.K
	Thermal diffusivity	α_{PVB}	1.878×10^{-7}	m^2/s
Water	Density	ρ_W	998	Kg/m^3
	Thermal conductivity	K_W	0.6	W/m.K
	Specific heat capacity	C_{pW}	4182	J/Kg.K
	Thermal diffusivity	α_W	1.438×10^{-7}	m^2/s

4.1. Heat transfer in a laminated glass during a fire

Figure 5 depicts the heat transfer model of a laminated glass during a fire. For our study, we selected a laminated glass panel measuring 0.6 m × 0.6 m, which comprises two glass layers and one PVB layer. The thicknesses of the glass and PVB are 6 mm and 0.38 mm, respectively. The laminated glass is divided into five surfaces in the *z*-direction (its thickness). Nine reading points were obtained from full-scale experiments [4,44] using thermocouples, which were distributed on the exposed surface from T1 to T9, as shown in Fig. 6(a). The non-uniform temperature distribution was calculated to mimic the actual thermal conditions of the experiment using these temperature measurements (T1 to T9), as shown in Fig. 6(b). The frame width surrounding the laminated glass is given by 20 mm.

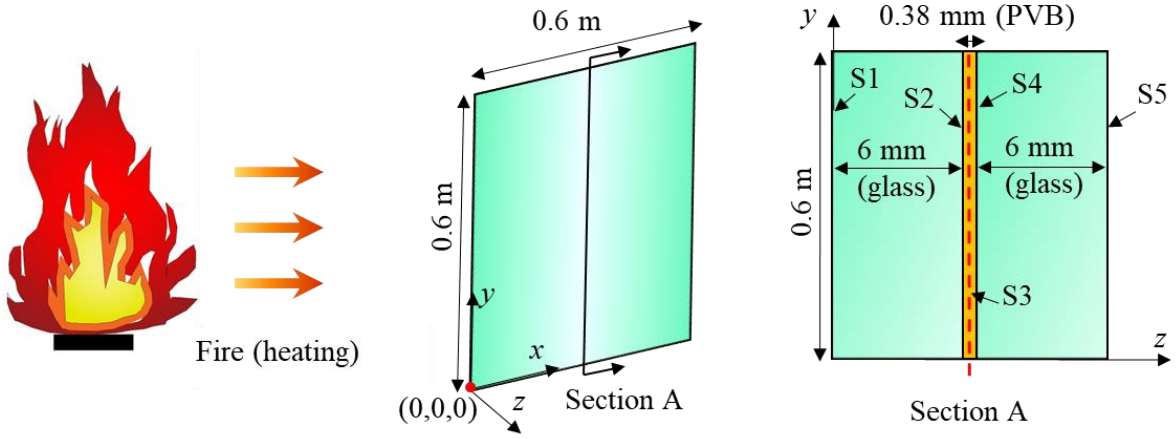

Fig. 5. Problem description diagram showing the geometric details of laminated glass, where the laminated glass consists of three layers (2 glass layers and 1 PVB layer) and 5 surfaces (S1 to S5) [4,44].

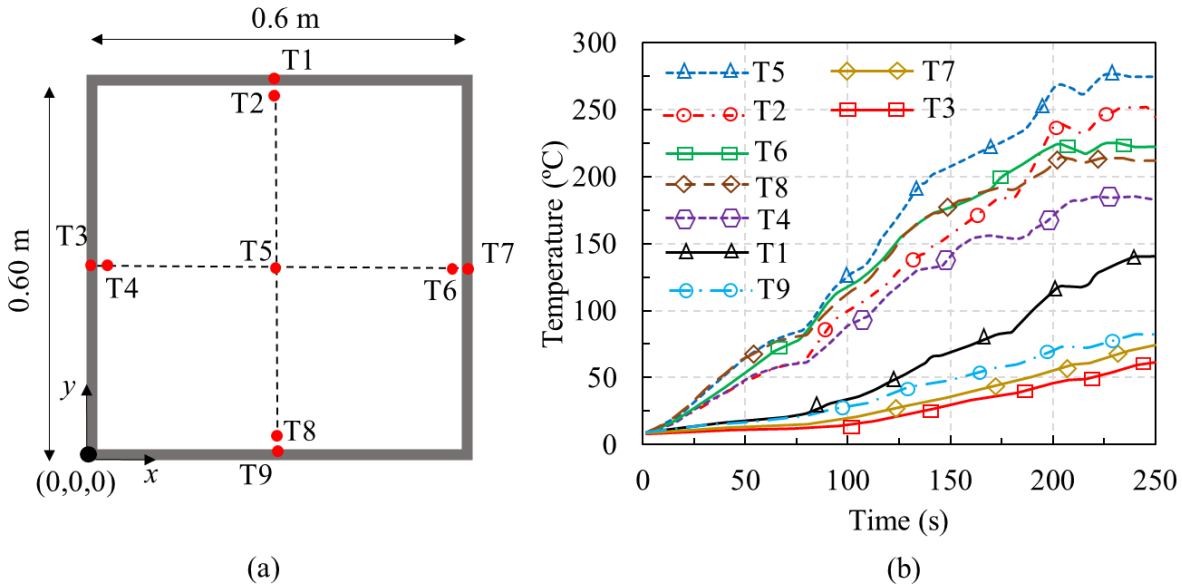

Fig. 6. Experimental temperature readings: (a) Locations of thermocouples at the exposed surfaces of laminated glass (T1 to T9) [4,44]; (b) Temperature variation over time [4,44].

To simulate the actual experimental scenario, temperature values are calculated at every point on the exposed glass to produce non-uniform temperature distribution. Here, we selected five reading points on the exposed glass and five on the frame (exposed surface), as shown in Fig. 6(a). Thus, the temperature is assumed to vary at every location according to the following

polynomial equations:

$$T_{e1}(x,y) = ax^2 + bx + cy^2 + dy + e \tag{32}$$

$$T_{e2}(x,y) = fx^2 + gx + hy^2 + iy \tag{33}$$

where T_{e1} and T_{e2} are the temperatures at the glass and frame locations, respectively; and a, b, c, d, e, f, g, h, and i are the polynomial coefficients which can be determined based on the experimental temperature readings at every time step as follows:

$$\begin{bmatrix} a \\ b \\ c \\ d \\ e \end{bmatrix} = \begin{bmatrix} x_2^2 & x_2 & y_2^2 & y_2 & 1 \\ x_4^2 & x_4 & y_4^2 & y_4 & 1 \\ x_5^2 & x_5 & y_5^2 & y_5 & 1 \\ x_6^2 & x_6 & y_6^2 & y_6 & 1 \\ x_8^2 & x_8 & y_8^2 & y_8 & 1 \end{bmatrix}^{-1} \begin{bmatrix} T2 \\ T4 \\ T5 \\ T6 \\ T8 \end{bmatrix} \tag{34}$$

$$\begin{bmatrix} f \\ g \\ h \\ i \end{bmatrix} = \begin{bmatrix} x_1^2 & x_1 & y_1^2 & y_1 \\ x_3^2 & x_3 & y_3^2 & y_3 \\ x_7^2 & x_7 & y_7^2 & y_7 \\ x_9^2 & x_9 & y_9^2 & y_9 \end{bmatrix}^{-1} \begin{bmatrix} T1 \\ T3 \\ T7 \\ T9 \end{bmatrix} \tag{35}$$

where x_1 to x_9 and y_1 to y_9 are the x and y coordinates, respectively, of the thermocouples. Eqs. (34) and (35) were solved by multiplying the inverse of thermocouples' coordinate matrices (Fig. 6(a)) with the vectors of experimental temperature readings (Fig. 6(b)), to obtain the polynomial coefficients (a, b, c, d, e, f, g, h, and i in Eqs. (32) and (33)). This procedure is then repeated at each time step.

4.2. Validation of heating and cooling behavior

We first validated our model in the heating scenario before proceeding to validate it in the cooling scenario with water film application. The glass and water layers are divided into six surfaces each, while the PVB layer is represented with a single surface (Fig. 3) because the PVB thickness (0.38 mm) is much lower than other material layers. The water layer of 1 mm

thickness is divided into six surfaces (*NWFS* = 6) to ensure it flows in a downward direction and remains exposed to the external heat flux once it is released. Note that the number of surfaces can be changed as shown in Section 4.3. Each surface is divided into 6400 particles (80 × 80). The *TNS* is equal to 13 and 19 in the heating (without water film) and cooling cases, respectively, and the *TNP* is equal to 83200 and 121600, in the heating and cooling cases, respectively. The same experimental conditions presented in Ref. [4,44] are applied in our 3DFDM and Autodesk CFD. However, the air convection in both Autodesk CFD and 3DFDM is represented by applying the heat transfer coefficient (h) with a value of 40 W/m^2 [44] at the ambient surface of the laminated glass, where the reference temperature (air temperature) is assumed to increase from 10 ºC to 70 ºC within 250 s of time simulation to consider the effects of air heating as in the experiment.

Fig. 7 shows the temperature variations as a function of time at the center of the ambient surface (TS5) using our 3DFDM in comparison to previous experimental results [4,44] and results obtained using Autodesk CFD and Abaqus [44]. This figure indicates that the temperature variation over time generated by our 3DFDM shows excellent agreement with the experimental results, thereby demonstrating the capability of our model to simulate the heat transfer problems. In addition, the temperature variation over time presented in [44] exhibits lower agreement with the experimental results in comparison to the temperature variations obtained using our 3DFDM and Autodesk CFD. The reason for this difference is that in [44], a uniform temperature was assumed by considering average temperature values at the exposed glass surface. However, in our study, we consider the non-uniform temperature distribution observed in the experiment, making our 3DFDM more realistic in simulating heat transfer in laminated glass when compared to other studies.

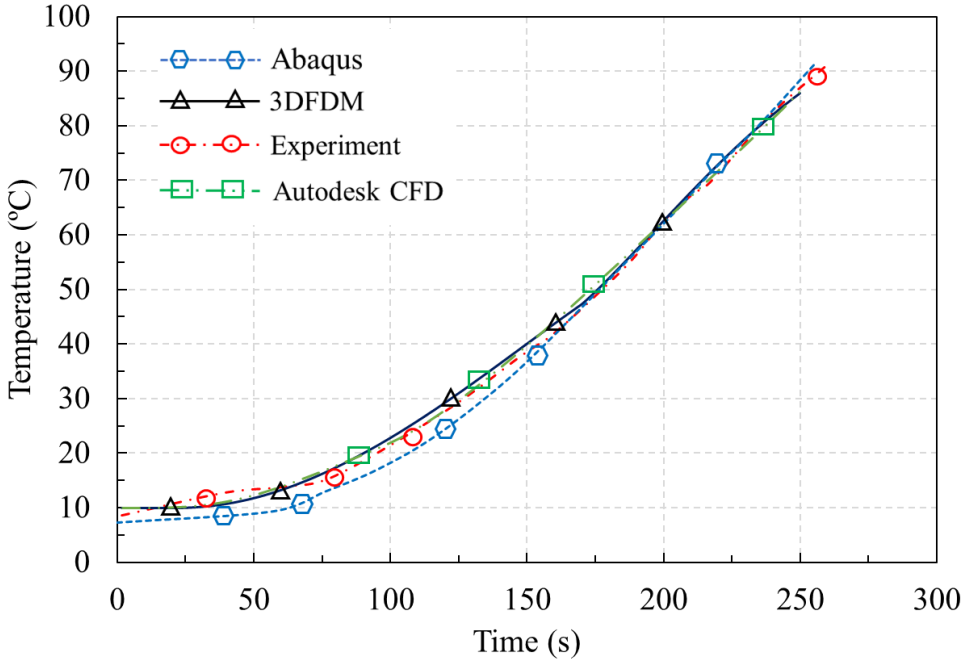

Fig. 7. Temperature variations as a function of time at the center of the ambient surface (TS5) using 3DFDM, experiments [4,44], Autodesk CFD, and Abaqus [44].

Next, we use our 3DFDM was to obtain the temperature distribution on other surfaces. Fig. 8 depicts the heat map of temperature (ºC) for the S1 to S5 surfaces of the laminated glass at 100 s and 200 s, respectively. The temperature values exhibit a significant difference at the first and second glass layers, especially between the exposed and ambient surfaces. This temperature difference increases with increasing heat. For example, the temperature difference at the center of the S1 and S5 surfaces (TS1 and TS5) is 108 ºC at 100 s, and it increases up to 196 ºC at 200 s as shown in Fig. 9. Furthermore, it should be noted that the temperature difference between TS2 and TS4 (before and after PVB layer) is approximately 30 ºC at 200 s.

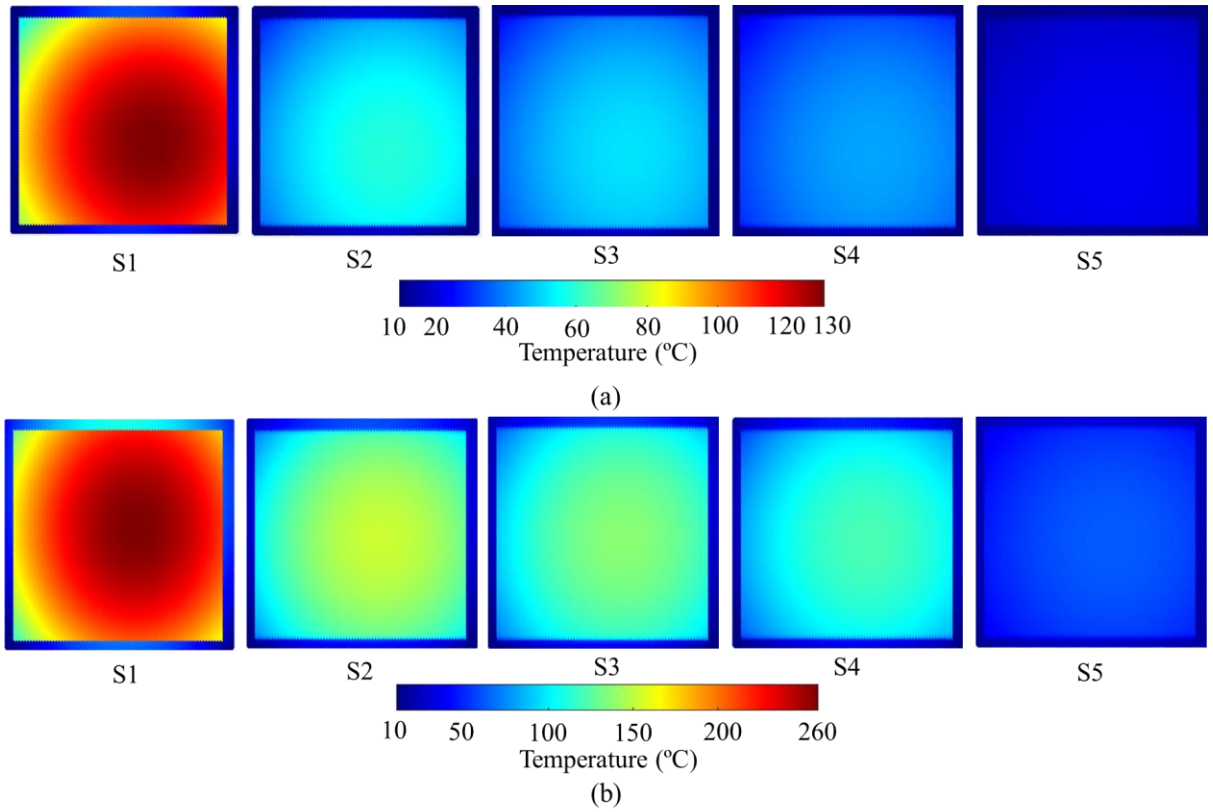

Fig. 8. Heat map of temperature (ºC) for surfaces S1 to S5 (a) at t = 100 s; (b) at t = 200 s.

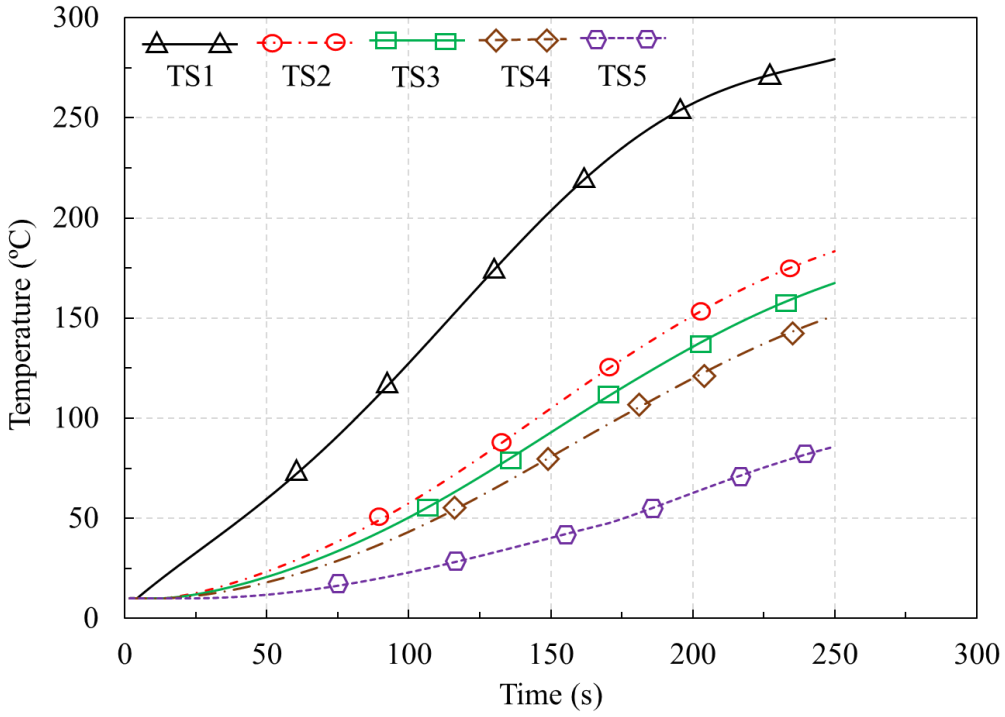

Fig. 9. Temperature variations as a function of time at TS1, TS2, TS3, TS4, and TS5 points (centers of S1 to S5 surfaces) when PVB thickness is 0.38 mm.

Table 3 summarizes the computational parameters for our 3DFDM and Autodesk CFD. It shows that although our 3DFDM uses 1.85 times more particles than the number of nodes used in Autodesk CFD, and Autodesk CFD uses 10 times more time steps than 3DFDM, our 3DFDM requires significantly less computational time. This is because both models have the same number of steps (2500), and our 3DFDM takes only 57 s to complete 2,500 numerical steps (250 s of thermal simulation), while Autodesk CFD takes 1200 s to complete the same number of numerical steps for the same simulation period. Besides, the computational cost per step and particle (CC_{SP}) is 2.74×10^{-7} s using our 3DFDM, compared to 1.07×10^{-5} s using Autodesk CFD. Therefore, our 3DFDM is 39 times faster than Autodesk CFD when the same number of steps and particles (nodes) were used for numerical simulation.

Table 3. Comparison of the computational parameters of 3DFDM and Autodesk CFD numerical models in laminated glass for the heating case

Item	3DFDM	Autodesk CFD
Number of particles/nodes	83200	44874
Time step (*TS*, s)	0.1	1
Total number of steps	2500	2500
Total simulation time (s)	250	250
Total computational cost (s)	57	1200
Computational cost (s) per second (CC_{SP})	2.74×10^{-7}	1.07×10^{-5}

The validation of our 3DFDM in the scenario of cooling by water film is illustrated in Fig. 10. The temperature drops during the cooling of the tempered glass experiment (one glass layer) [45] were used for validation. The temperature variation over time at the exposed surface was applied in [45], as shown in Fig. 10(a). The required point is located under the top of the glass (y = 0.57 m), where the water film is released at 278 s when the temperature reaches around 310 ºC. Since the thermocouple readings in the experiment were affected by the down-flowing water film, the temperature variation over time in our 3DFDM was calculated based on the average temperature values of the exposed glass particles and the adjacent heated water film particles. As depicted in Figs. 10, the temperature variations over time at the exposed and ambient surfaces produced by 3DFDM agree better with experimental measurements than those obtained from Autodesk CFD, especially in the cooling case.

It can be observed from Fig. 10 that cooling occurs more sharply (i.e., the temperature drops more rapidly) using Autodesk CFD compared to our 3DFDM. This may be due to our model's ability to track the thermal behavior of down-flowing water film particles rather than the control volume technique employed in Autodesk CFD. Moreover, the effect of evaporation can be effectively prevented in our 3DFDM, and the water film is activated gradually in a more realistic manner (i.e., activated at each particle separately). However, the mechanism for preventing evaporation in Autodesk CFD is not clear, and water film activation is executed suddenly for all particles. These comparisons further demonstrate the rationality and accuracy of our 3DFDM to simulate the cooling behavior.

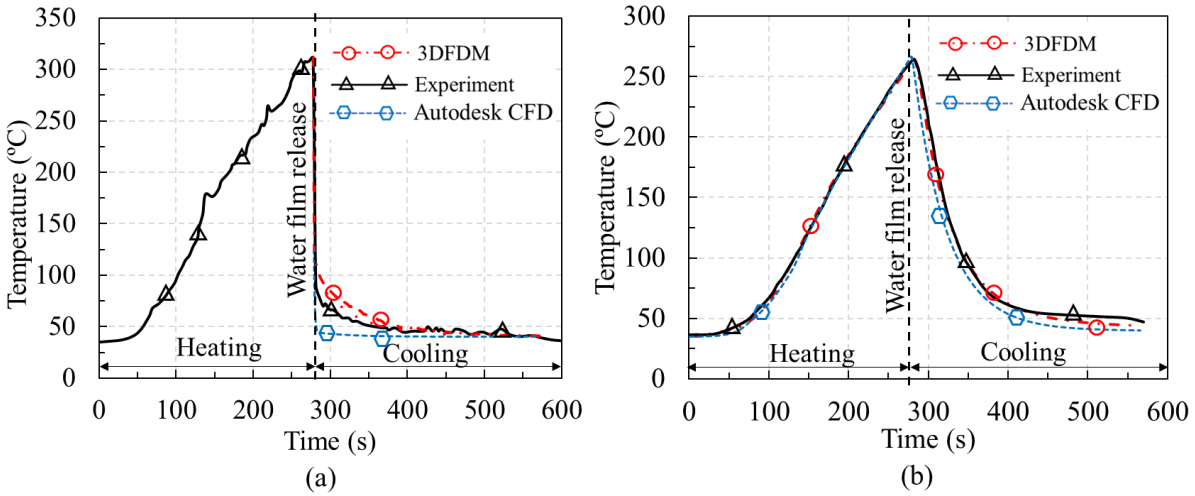

Fig. 10. Temperature variations over time in the heating and cooling cases using our 3DFDM, experiment [45], and Autodesk CFD at exposed and ambient surfaces, where the water film is released at 278 s with a down-flowing velocity of 0.645 m/s and a thickness value of 0.5 mm [45]: (a) At exposed surface; (b) At ambient surface.

Table 4 summarizes the computational parameters used in both our 3DFDM and Autodesk CFD. In this case, the processing speed of our 3DFDM (using 63,536 particles) is about 71 times faster than that of Autodesk CFD (using 12,077 particles). Note that the *TS* used in Autodesk CFD is 0.1 s, whereas the *TS* used in our 3DFDM is 0.0124 s since it is calculated according to Eq. (31). Therefore, the *TS* value utilized in our model is less than the *TS* value used in Autodesk CFD. Besides, our 3DFDM requires only 228 s to execute 288 s of the entire simulation period, whereas the Autodesk CFD takes 16,200 s to accomplish the same period.

418 Table 4. Comparison of the computational parameters of 3DFDM and Autodesk CFD
419 numerical models in single glass layer for the cooling case

Item	3DFDM	Autodesk CFD
Number of particles/nodes	63536	12077
Time step (*TS*, s)	0.0124	0.1
Number of total steps	23226	28800
Total simulation time (s)	288	288
Total computational cost (s)	228	16200
Computational cost (s) per second	0.79	56.25
CC_{SP}	1.54×10^{-7}	4.66×10^{-5}

420 *4.3. Cooling mechanism of the laminated glass facade*

421 The cooling behavior and their underlying mechanisms of laminated glass facade were
422 investigated considering the PVB thickness of 0.38 mm. First, the thermal interaction between
423 cold adjacent water film particles and the exposed hot glass surface were examined, as shown
424 in Fig. 11. It can be observed that when water film particles are released at t = 100 s and with
425 a down-flowing velocity of 0.7 m/s, a sudden drop in temperature at the exposed glass is
426 recorded. As shown in the contour plots, the temperature at the center of the exposed glass
427 surface (TS1) drops from 121.5 ºC to around 83 ºC (i.e., a drop of around 38 ºC) at 100.76 s
428 (after 0.76 s from water film release). The temperature drop in the glass increases when the
429 point is located at the upper parts (y = 0.6 m), as the water film is released at this location. The
430 temperature of the adjacent water film particles increases from 10 ºC to around 70 ºC at t =
431 100.76 s. It is worth noting that the temperature of the water film is less than 100 ºC when the
432 down-flowing velocity is 0.7 m/s; therefore, no evaporation of the water film is apparent in this
433 case.

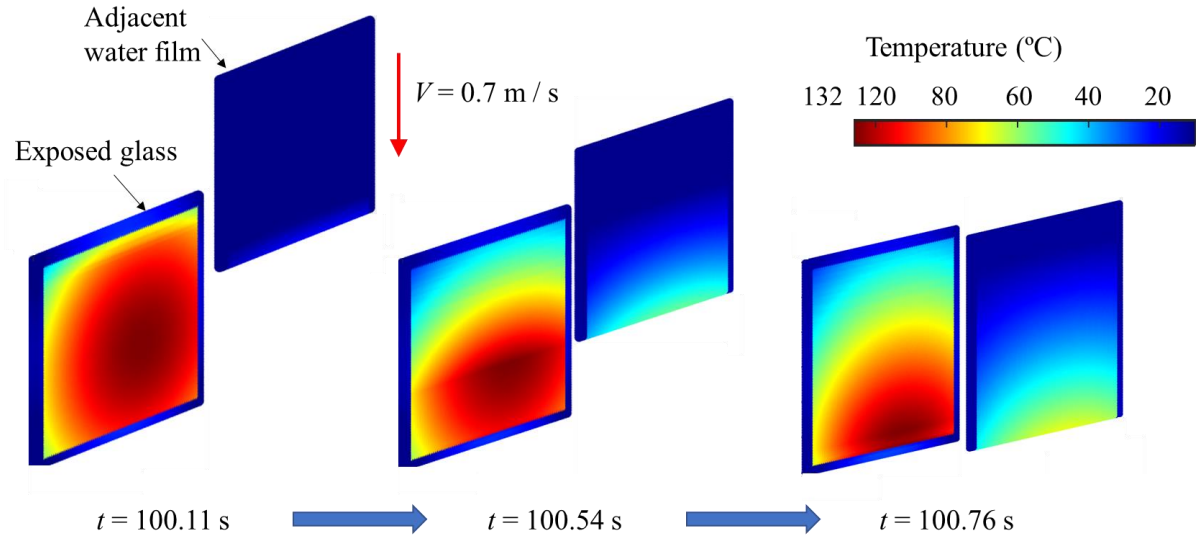

Fig. 11. Heat map of the temperature of exposed glass surface (S1) and adjacent water film surface at several time instants (t = 100.11 s, t = 100.54 s, t = 100.76 s) when water film is released at t = 100 s with a down-flowing velocity of 0.7 m/s.

When the temperature of the exposed glass surface (S1) drops due to water film application, the cooling continues for other surfaces but at a lower rate, as depicted in Figs. 12 and 13. For instance, the temperature at the center of the exposed glass surface (TS1) drops from 121.5 ºC to 44.7 ºC within only 8 s. By contrast, the temperature at the center of the S4 surface (TS4) drops from 43.5 ºC to around 32 ºC within 80 seconds. Therefore, the temperature drop at the exposed surface is steeper compared to other surfaces. The results in Figs. 12 and 13 also demonstrate that the surfaces located near the ambient side of laminated glass are influenced by cooling more slowly when compared to the exposed surface. For example, the cooling at the exposed surface of laminated glass occurs immediately when the water film is released (t = 100 s), however, the cooling at S5 surface occurs after 45 s from water film release (t = 145 s) as shown in Fig. 12. Moreover, when water film is released at the exposed surface of laminated glass, the heating continues for other surfaces at different time durations depending on the surface's location. For example, the heating at S5 surface is continuous for 45 s after the water film is released, where the temperature at the center of S5 surface (TS5) increases from around 24 °C at t = 100 s (water film release time) to 36.89 °C at t = 145 s.

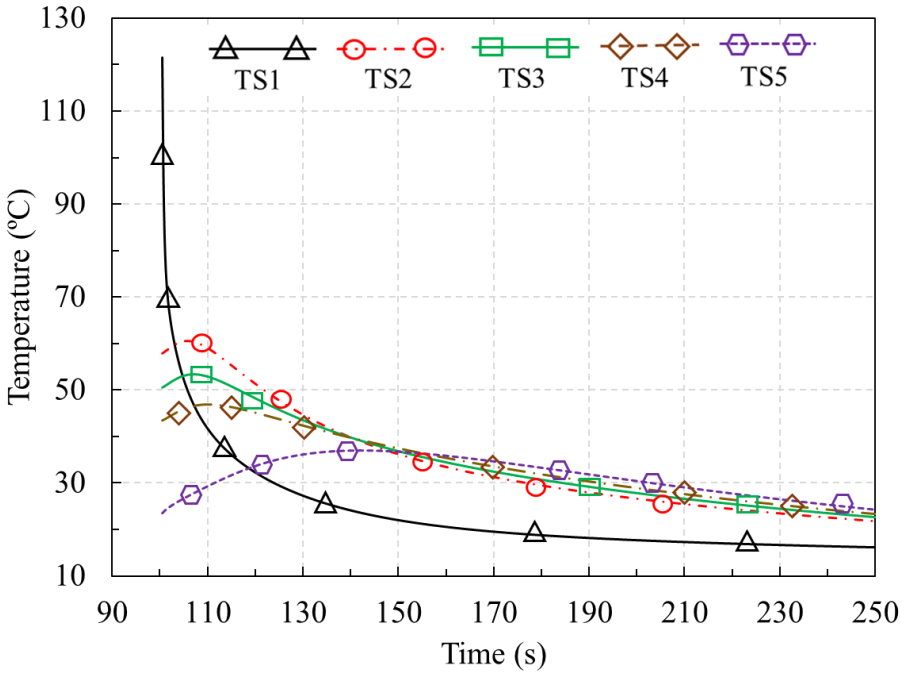

453

454 Fig. 12. Temperature variations over time at points TS1 to TS5 (centers of S1 to S5 surfaces)

455 when water film is released at t = 100 s.

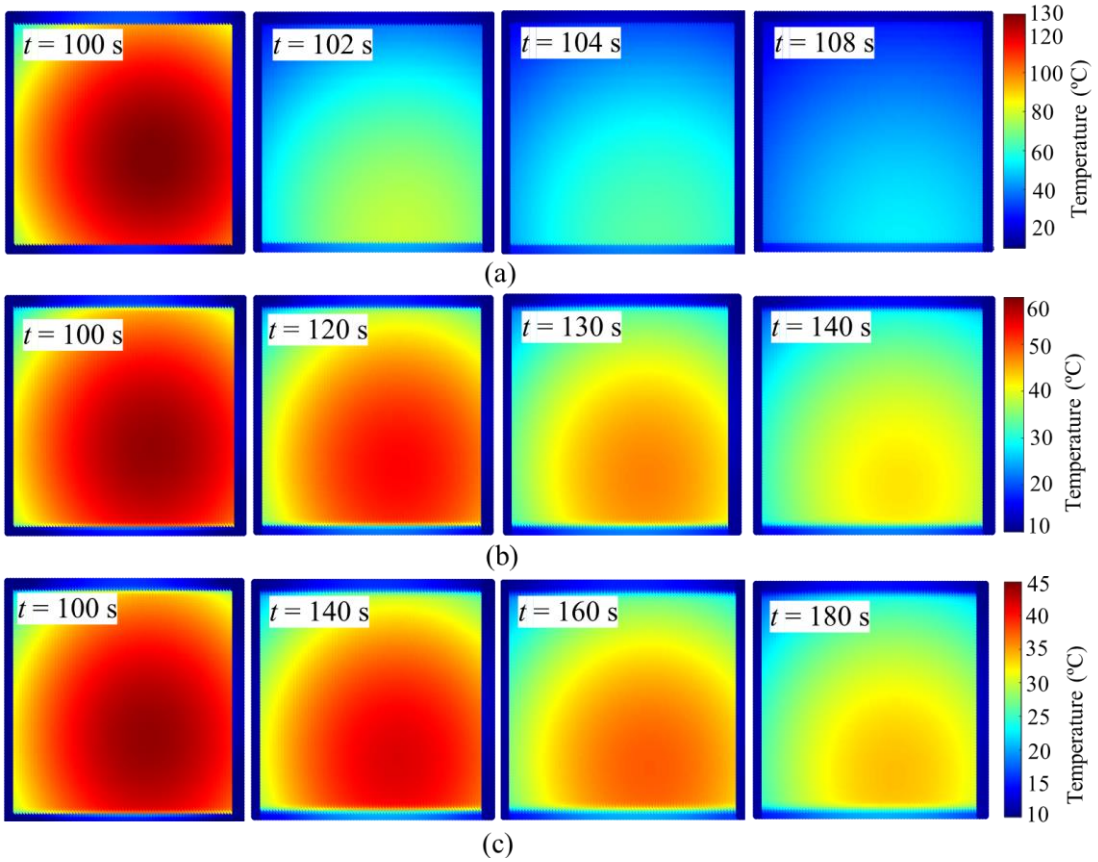

456

457 Fig. 13. Heat map of the temperature (ºC) of laminated glass surfaces at several time steps

458 when water film is released at t = 100 s: (a) S1 surface (exposed); (b) S2 surface; (c) S4 surface.

The effects of 3DFDM parameters such as *NPS*, *NWFS,* and *TS* were also examined. Fig. 14(a) shows temperature variations as a function of time at point TS2 (center of surface S2). When *NPS* increases from 4900 to 8100, *TS* decreases from 0.0124 s to 0.0096 s because the spacing between particles (spacing at *y*-direction) decreases. Fig. 14(b) shows the heat map of different *NPS* at t = 130 s. It can be concluded that the effects of changing *TS* and *NPS* are negligible in our model because the *TS* is calculated based on the spacing of particles and, therefore, on *NPS* (Eq. (31)) where each water film particle interacts with one glass particle at each step according to the *TS* calculation scheme and the 3DFDM illustrated in Section 3. Moreover, the activation of cooling by water film is conducted at each particle of the exposed glass surface rather than sudden cooling activation for all particles.

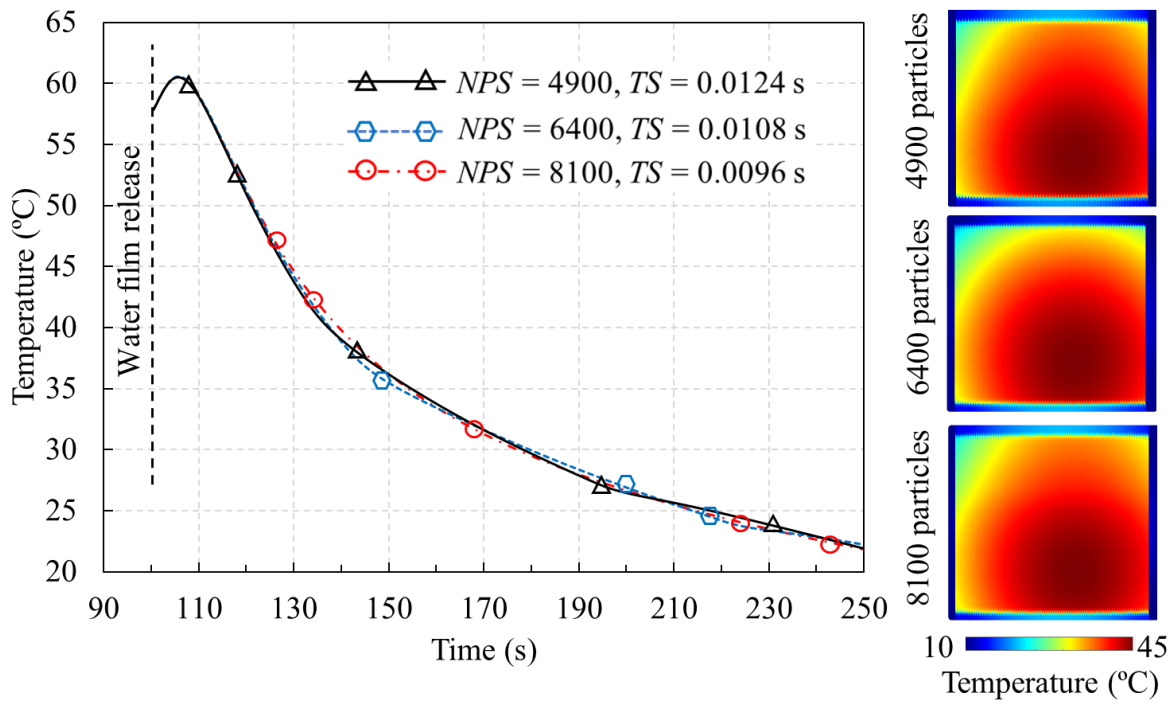

Fig. 14. Effects of *NPS* and *TS* on our 3DFDM in the cooling case when water film is applied at t = 100 s: (a) Temperature variations as a function of time at point TS2 when *NPS* values are 4900, 6400, and 8100; (b) Heat map of temperature at t = 130 s when *NPS* values are 4900, 6400, and 8100.

The effects of increasing the *NWFS* were studied as shown in Fig. 15. When *NWFS* increases at the same value of *NPS*, the temperature drop decreases because increasing *NWFS* requires more time for our 3DFDM to capture the cooling effects of the additional *NWFS*. For example, when *NWFS* increases from 6 to 7 at the same *NPS* (6400), the temperature drop decreases, as shown in Fig. 15. The temperature values at 167 s are 33 ºC and 34 ºC when *NWFS* values are 6 and 7, respectively, at *NPS* = 6400. Even though the temperature difference is small (1 ºC), increasing the *NPS* and thus decreasing *TS* will reduce that temperature difference, as shown in Fig. 15. When *NPS* increases from 6400 to 10,000 at *NWFS* = 7, the temperature variation approaches the temperature variation when *NPS* and *NWFS* are 6400 and 6, respectively. Therefore, a greater *NWFS* requires a smaller *TS* to capture the thermal transfer when the number of surfaces is increased.

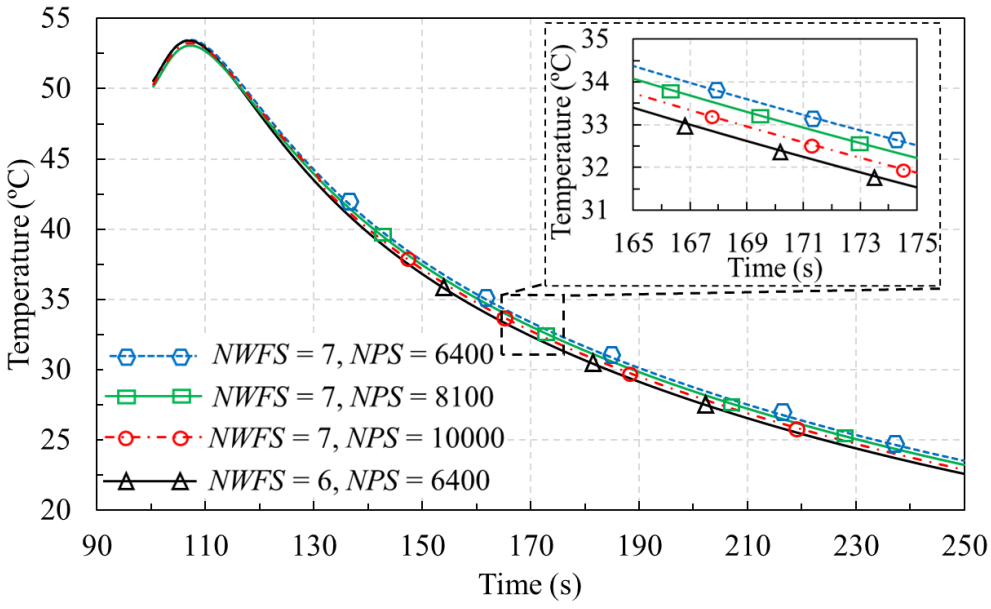

Fig. 15. Temperature variations as a function of time when *NPS* values are 6400, 8100, and 10,000 and when *NWFS* is varied from 6 to 7 surfaces.

4.4. Effects of PVB thickness on thermal and cooling behavior of laminated glass

The effects of PVB thickness on the thermal behavior of laminated glass are illustrated in Fig. 16(a). It is notable that as PVB thickness increases from 0.38 mm to 0.76 mm or from 0.76 mm to 1.14 mm, the temperature at the center of the second glass layer near the PVB (TS4) drops around 6.5 ºC to 7.5 ºC. Fig. 16(b) shows the heat map of the surface temperature (TS4)

at t = 200 s, which are 119.7 ºC, 113.2 ºC, and 105.7 ºC when the PVB thicknesses are 0.38 mm, 0.76 mm, and 1.14 mm, respectively. Therefore, for each 0.38 mm increment in PVB thickness results to temperature decreases in the second layer of about 7 ºC. Furthermore, when t is less than 150 s, the temperature at the second glass layer (TS4) is less than approximately 70 ºC, and therefore, the temperature differences between several PVB thickness cases are minimal. The delay in heating is justified by the fact that heat transport through the laminated glass thickness requires more time to reach the second layer, and fire requires more time to mature and to generate higher temperature values.

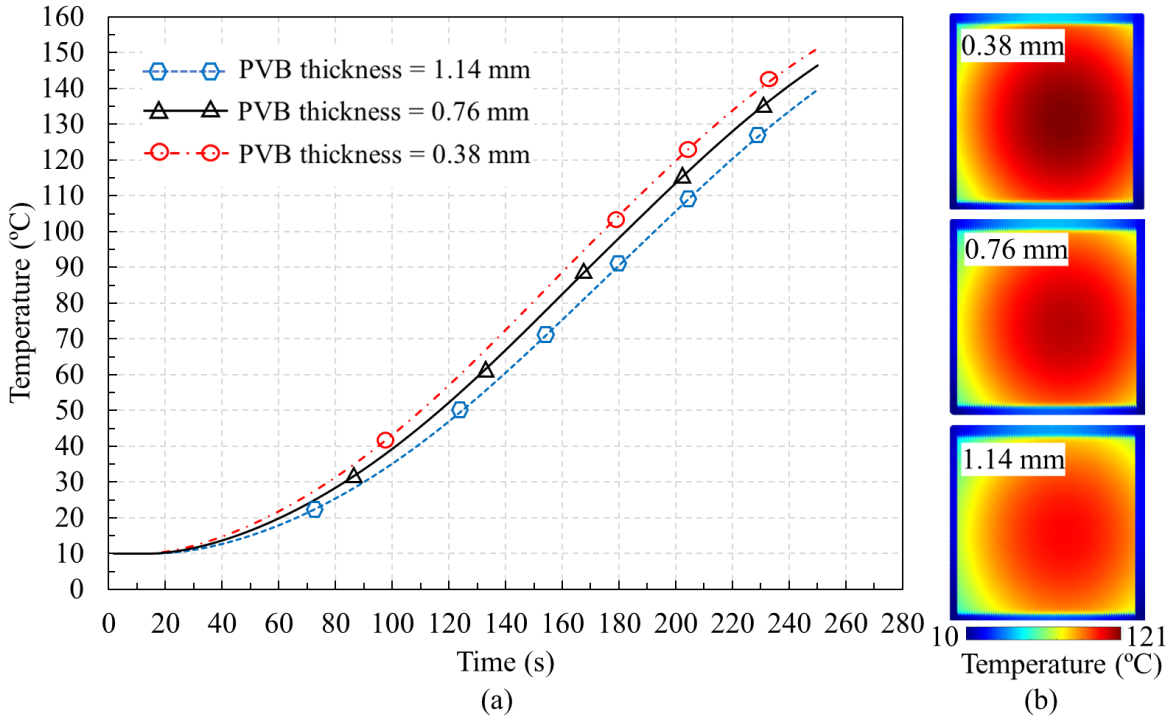

Fig. 16. Effects of PVB thickness on the thermal behavior of laminated glass in the heating case: (a) Temperature variations over time when PVB thicknesses are 0.38 mm, 0.76 mm, and 1.14 mm at the center of surface S4 (TS4); (b) Heat map of the temperature of surface S4 at t = 200 s when PVB thicknesses are 0.38 mm, 0.76 mm, and 1.14 mm.

Next, we examined the effects of varying PVB thickness on the cooling behavior of laminated glass. Fig. 17(a) shows the temperature variations over time after applying the water film at t = 100 s with PVB thicknesses of 0.38 mm, 0.76 mm, and 1.14 mm at the center of the S4 surface (TS4). Fig. 17(b) shows the heat map of the temperature at different PVB

thicknesses at t = 125 s. Notably, a small delay is apparent in the cooling of the second glass layer when the PVB thickness increases. PVB thickness increasing from 0.38 mm to 0.76 mm or from 0.76 mm to 1.14 mm delays the cooling process by about 4 s—the temperature begins to fall at 110 s, 113.7 s, or 117.6 s, respectively, at TS4. Thus, we conclude that adding 0.38 mm to PVB thickness results in a delay of around 4 s in cooling time.

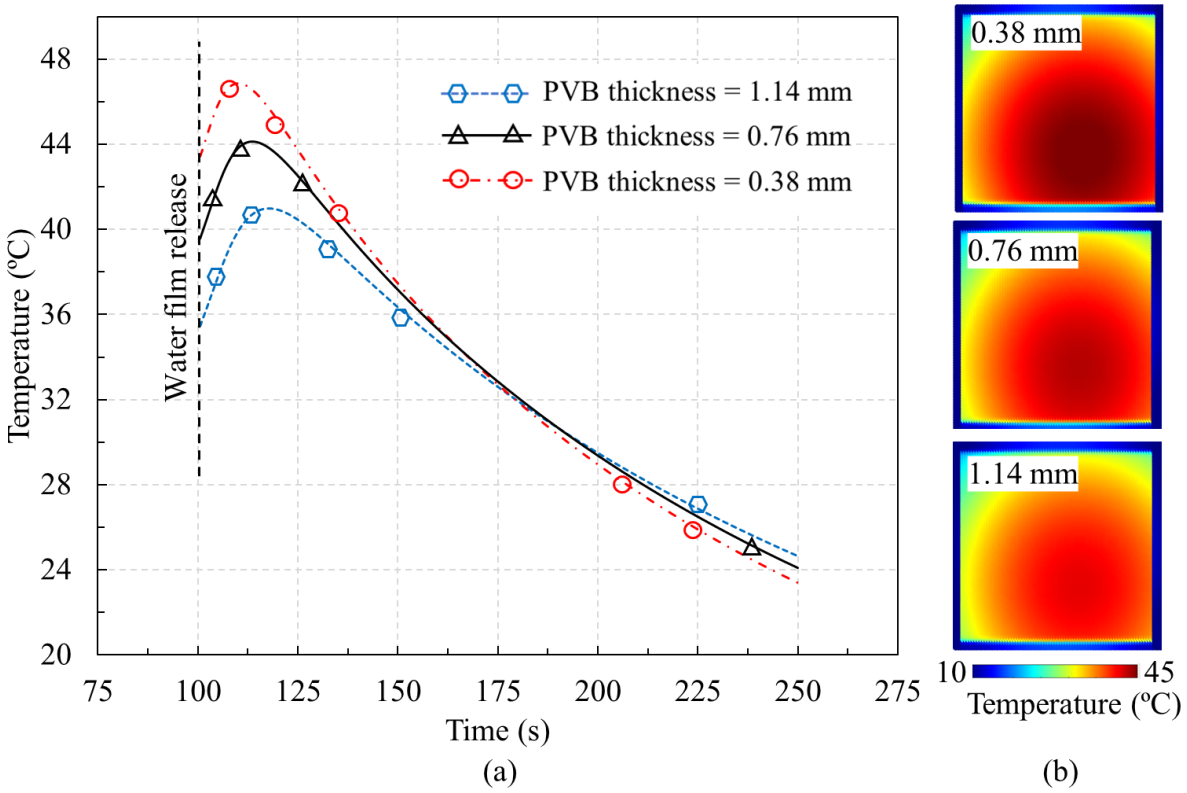

Fig. 17. Effects of PVB thickness on the thermal behavior of laminated glass in the cooling case when water film is applied at t = 100 s: (a) Temperature variations over time with PVB thicknesses of 0.38 mm, 0.76 mm, and 1.14 mm; (b) Heat map of temperature at t = 125 s with PVB thicknesses of 0.38 mm, 0.76 mm, and 1.14 mm.

4.5. Effects of WFRT on the cooling behavior of laminated glass

To provide general guidelines on the best time to apply a water film to protect laminated glass from failure, the effects of water film release time (WFRT) on the thermal and cooling behavior of laminated glass are examined here in detail. Three WFRT values (75 s, 100 s, and 150 s) and four different points (TS1, TS2, TS4, and TS5) are considered. Fig. 18 and Table 5

illustrate the effects of WFRT on the cooling behavior of laminated glass at TS1, TS2, TS4, and TS5. For instance, Fig. 18(a) shows the temperature variations as a function of time at point TS1 when a water film is applied at 75 s, 100 s, and 150 s. Table 5 shows the temperature and cooling rate values at different values of WFRT. The cooling rate at the exposed surface was measured within 25 s; for the other surfaces, it was measured within 125 s, since the temperature drop at the exposed surface is much steeper.

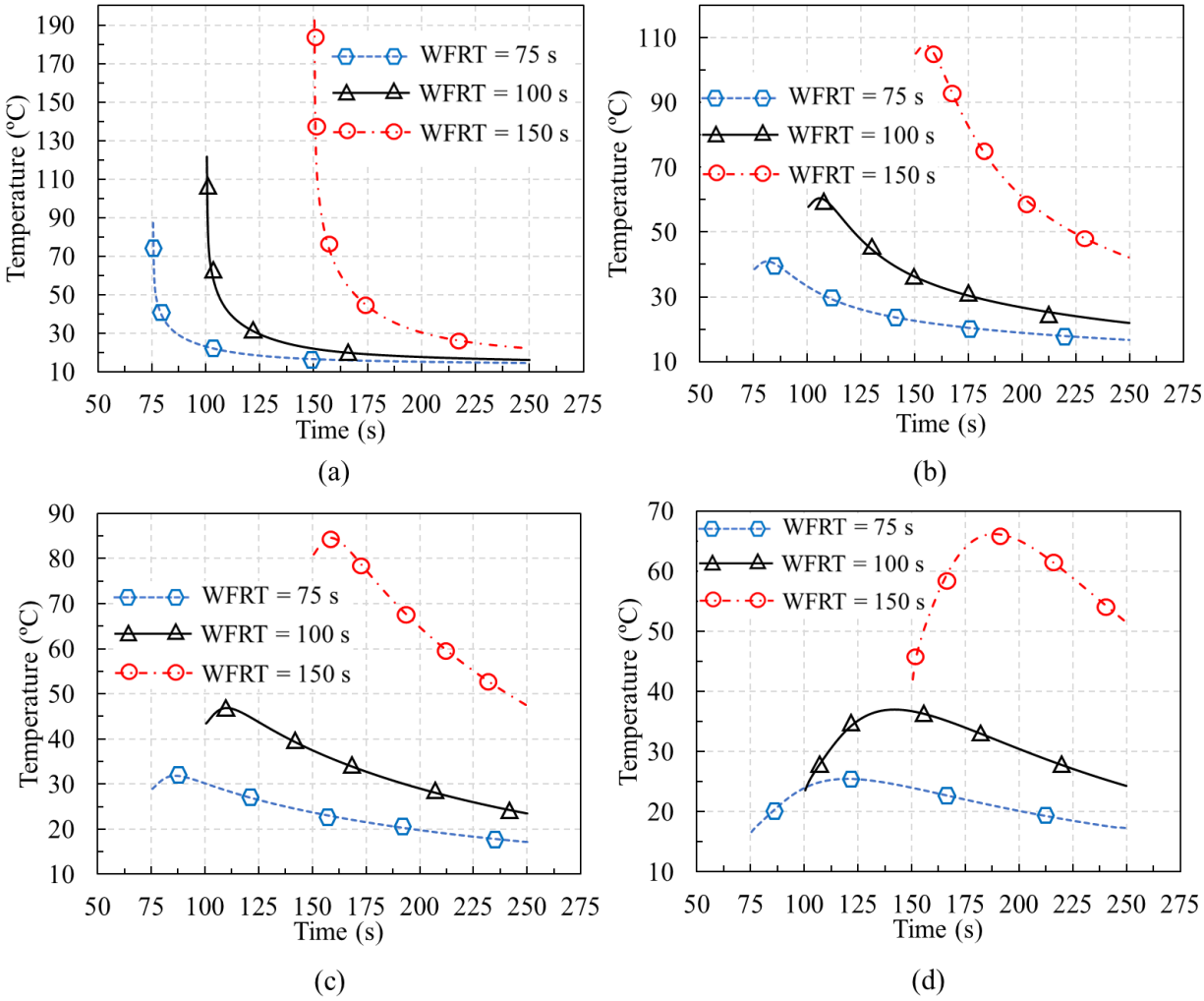

Fig. 18. Effects of WFRT on the cooling behavior of laminated glass when a water film is applied at t = 75 s, t = 100 s, and t = 150 s: (a) At point TS1 (center of S1 surface); (b) At point TS2 (center of S2 surface); (c) At point TS4 (center of S4 surface); (d) At point TS5 (center of S5 surface).

538 Table 5. Summary of temperature and cooling rate values at TS1, TS2, TS4, and TS5 when
539 WFRT values vary from 75 s to 150 s.

Location	WFRT (s)	Temperature (T, ºC)		Cooling rate (ºC/s)
TS1		At t = WFRT	At t = WFRT + 25 s	
	75	87.41	23.12	2.57
	100	121.48	29.34	3.69
	150	192.23	44.11	5.92
TS2		At t = WFRT + 6 s	At t = WFRT + 125 s	
	75	41.06	18.86	0.19
	100	60.49	23.93	0.31
	150	107.55	42.08	0.7
TS4		At t = WFRT + 11 s	At t = WFRT + 125 s	
	75	31.87	19.8	0.11
	100	46.84	25.9	0.18
	150	84.16	47.39	0.41
TS5		At t = WFRT +45 s	At t = 250 s	
	75	25.41	17.24	0.06
	100	36.89	24.3	0.12
	150	65.85	51.51	0.26

540 Based on the simulated results of the effects of WFRT on the cooling behavior of laminated
541 glass in Fig. 18 and Table 5, the following results are presented: (1) Cooling rates decrease with
542 decreasing WFRT since there will be less temperature drop when water films are applied early
543 in the fire. For example, at TS1, the temperature drops from 87.41 ºC to 23.12 ºC within 25 s
544 when WFRT is 75 s, whereas it drops from 192.23 ºC to 44.1 ºC when WFRT is 150 s, as shown
545 in Fig. 18(a). Therefore, the cooling rate decreases from 5.92 ºC/s to 2.57 ºC/s when the WFRT
546 decreases from 150 s to 75 s. (2) The effects of WFRT on the cooling rate decrease dramatically
547 when moving away from the exposed surface toward the ambient surface. For instance, the
548 cooling rates at WFRT = 100 s are 3.69 ºC/s, 0.31 ºC/s, 0.18 ºC/s, and 0.12 ºC/s at TS1, TS2,
549 TS4, and TS5, respectively, as shown in Table 5. Therefore, the cooling rate at the exposed
550 surface plays an important role in laminated glass fracture since the crack initiates at the
551 exposed surface due to a high cooling rate (when water film is applied late), and it can
552 propagate to other surfaces. (3) The effects of water film cooling start to take place after 45 s
553 at the ambient surface (TS5), as shown in Fig. 18(d), while cooling occurs immediately at the

554 exposed glass surface. The surfaces S2 and S4 adjacent to the PVB layer start cooling after 6 s
555 and 11 s from WFRT at the same PVB thickness, as shown in Figs. 18(b) and 18(c).

556 ## 5. Conclusions

557 In this paper, we proposed a three-dimensional finite difference method (3DFDM) to
558 accurately simulate the heating and cooling behaviors of laminated glass facades exposed to
559 fire and down-flowing water film. We utilized our 3DFDM to model the thermal and cooling
560 response mechanism of laminated glass under the influence of fire and water film, and
561 successfully validated the model by comparing the results with previous experimental data and
562 results obtained using commercial software packages. Our 3DFDM demonstrated high
563 computational efficiency and accuracy in accurately simulating the heating and cooling phases
564 that occur in real fire scenarios.

565 The proposed modeling technique was then applied to investigate the effects of PVB
566 thickness on the heating and cooling behaviors of laminated glass, with a particular interest in
567 the temperature of the second glass layer (ambient surface). The simulated results show that
568 every 0.38 mm increment in PVB thickness decreases the temperature in the second glass layer
569 by around 7 ºC. Moreover, the cooling of the second glass layer is delayed by around 4 s when
570 the PVB thickness increases by 0.38 mm. Finally, the effects of water film release time (WFRT)
571 on the cooling behavior of laminated glass were investigated to examine the cooling rate at
572 different surfaces of the laminated glass. It was found that the cooling rate is much higher on
573 the exposed surface when compared to other surfaces, especially the ambient surface. Moreover,
574 the cooling rate increases when the WFRT increases.

575 Besides, our numerical results demonstrated that WFRT has more impact on the cooling
576 behavior of laminated glass than PVB thickness. Accordingly, the early release of a water film
577 is the most important procedure to protect laminated glass from failure. The outputs of this
578 study can be used to examine the thermal and fracture behaviors of laminated glass, thus
579 providing guidance on the optimum water film parameters (including WFRT) to protect against
580 the failure of laminated glass during a fire incident. The proposed 3DFDM can be applied to
581 study the thermal behaviors of other solids and composites during a fire.

Declaration of competing interest

The authors declare that they have no known competing financial interests or personal relationships that could have appeared to influence the work reported in this paper.

CRediT authorship contribution statement

D.A. Abdoh: Methodology, Formal analysis, Writing - original draft. **Y. Zhang:** Formal analysis, Writing - review & editing. **A.S. Ademiloye:** Formal analysis, Writing - review & editing. **V.K.R. Kodur:** Writing - review & editing. **K.M. Liew:** Conceptualization, Resources, Project administration, Supervision, Writing - review & editing.

Acknowledgments

The authors gratefully acknowledge the supports provided by the Research Grants Council of the Hong Kong Special Administrative Region, China (Project No. 9043135, CityU 11202721). The first author, D.A. Abdoh under the supervision of Professor K.M. Liew, acknowledges the UGC-Postgraduate Studentship awarded by the Hong Kong Government to support his PhD program in the Department of Architecture and Civil Engineering, City University of Hong Kong, Hong Kong, China.

References

[1] Bedon C. Structural Glass Systems under Fire: Overview of Design Issues, Experimental Research, and Developments. Adv Civ Eng 2017;2017. https://doi.org/10.1155/2017/2120570.

[2] Grant G, Brenton J, Drysdale D. Fire suppression by water sprays. Prog Energy Combust Sci 2000;26:79–130. https://doi.org/10.1016/S0360-1285(99)00012-X.

[3] Hu WC, Nurcholik SD, Lee SK, Lin TH. Evaluations on heat resistance of curtains with water film in a fire. J Chinese Inst Eng Trans Chinese Inst Eng A 2016;39:615–22. https://doi.org/10.1080/02533839.2016.1146092.

[4] Wang Y, Wang Q, Wen JX, Sun J, Liew KM. Investigation of thermal breakage and heat transfer in single, insulated and laminated glazing under fire conditions. Appl Therm Eng 2017;125:662–72. https://doi.org/10.1016/j.applthermaleng.2017.07.019.

[5] Wang Y, Wang Q, Sun J, He L, Liew KM. Influence of fire location on the thermal performance of glass façades. Appl Therm Eng 2016;106:438–42. https://doi.org/10.1016/j.applthermaleng.2016.06.057.

[6] Wang Y, Wang Q, Shao G, Chen H, Su Y, Sun J, et al. Experimental study on thermal breakage of four-point fixed glass façade. Fire Saf Sci 2014;11:666–76. https://doi.org/10.3801/IAFSS.FSS.11-666.

[7] Wang Y, Wu Y, Wang Q, Liew KM, Chen H, Sun J, et al. Numerical study on fire response of glass facades in different installation forms. Constr Build Mater 2014;61:172–80. https://doi.org/10.1016/j.conbuildmat.2014.03.012.

[8] Bakalakos S, Kalogeris I, Papadopoulos V. An extended finite element method formulation for modeling multi-phase boundary interactions in steady state heat conduction problems. Compos Struct 2021;258:113202. https://doi.org/10.1016/j.compstruct.2020.113202.

[9] Peijian D, Li C, Xiang D, Junbo X, Junling L, Wei J, et al. Multiscale analysis on the anisotropic thermal conduction of laminated fabrics by finite element method. Compos Struct 2022;292. https://doi.org/10.1016/j.compstruct.2022.115672.

[10] Ibouroi LA, Vidal P, Gallimard L, Ranc I. Thermal analysis of composite beam structure based on a variable separation method for any volume heat source locations and temporal variations. Compos Struct 2022;300. https://doi.org/10.1016/j.compstruct.2022.116154.

[11] Costa R, Nóbrega JM, Clain S, Machado GJ. Very high-order accurate polygonal mesh finite volume scheme for conjugate heat transfer problems with curved interfaces and imperfect contacts. Comput Methods Appl Mech Eng 2019;357:112560. https://doi.org/10.1016/j.cma.2019.07.029.

[12] Farmaga I, Shmigelskyi P, Spiewak P, Ciupinski L. Evaluation of computational complexity of finite element analysis. 2011 11th Int Conf - Exp Des Appl CAD Syst Microelectron CADSM 2011 2011:213–4.

[13] Calo VM, Collier NO, Pardo D, Paszynski MR. Computational complexity and memory usage for multi-frontal direct solvers used in p finite element analysis. Procedia Comput Sci 2011;4:1854–61. https://doi.org/10.1016/j.procs.2011.04.201.

[14] Ewing RE, Lin T, Lin Y. On the accuracy of the finite volume element method based on piecewise linear polynomials. SIAM J Numer Anal 2002;39:1865–88. https://doi.org/10.1137/S0036142900368873.

[15] Ye X. Analysis and convergence of finite volume method using discontinuous bilinear functions. Numer Methods Partial Differ Equ 2008;24:335–48. https://doi.org/10.1002/num.20266.

[16] Li Z, Sheikholeslami M, Chamkha AJ, Raizah ZA, Saleem S. Control volume finite element method for nanofluid MHD natural convective flow inside a sinusoidal annulus under the impact of thermal radiation. Comput Methods Appl Mech Eng 2018;338:618–33. https://doi.org/10.1016/j.cma.2018.04.023.

[17] Sciberras T, Demicoli M, Grech I, Mallia B, Mollicone P, Sammut N. Coupled finite element-finite volume multi-physics analysis of MEMS electrothermal actuators. Micromachines 2022;13. https://doi.org/10.3390/mi13010008.

[18] Casadei F, Leconte N, Coupling finite elements and finite volumes by Lagrange multipliers for explicit dynamic fluid–structure interaction, Int. J. Numer. Meth. Engng.2011; 86:1-17.

[19] Shahrzadi M, Davazdah Emami M, Akbarzadeh AH. Heat transfer in BCC lattice materials: Conduction, convection, and radiation. Compos Struct 2022;284:115159. https://doi.org/10.1016/j.compstruct.2021.115159.

[20] Tang L, Gao T, Song L, Meng L, Zhang C, Zhang W. Topology optimization of nonlinear heat conduction problems involving large temperature gradient. Comput Methods Appl Mech Eng 2019;357:112600. https://doi.org/10.1016/j.cma.2019.112600.

[21] Yaji K, Yamasaki S, Fujita K. Data-driven multifidelity topology design using a deep generative model: Application to forced convection heat transfer problems. Comput Methods Appl Mech Eng 2022;388:114284. https://doi.org/10.1016/j.cma.2021.114284.

[22] Idesman A, Dey B. A high-order numerical approach with Cartesian meshes for modeling of wave propagation and heat transfer on irregular domains with inhomogeneous materials. Comput Methods Appl Mech Eng 2020;370:113249. https://doi.org/10.1016/j.cma.2020.113249.

669 [23] Albatayneh A, Alterman D, Page A, Moghtaderi B. The Significance of Time Step Size
670 in Simulating the Thermal Performance of Buildings. Adv Res 2015;5:1–12.
671 https://doi.org/10.9734/air/2015/20223.
672 [24] Naboni E, Lee DS, Fabbri K. Thermal Comfort-CFD maps for Architectural Interior
673 Design. Procedia Eng 2020;180:110–7. https://doi.org/10.1016/j.proeng.2017.04.170.
674 [25] Zhang LW, Lei ZX, Liew KM. Computation of vibration solution for functionally graded
675 carbon nanotube-reinforced composite thick plates resting on elastic foundations using
676 the element-free IMLS-Ritz method. Appl Math Comput 2015;256:488–504.
677 https://doi.org/10.1016/j.amc.2015.01.066.
678 [26] Zhang LW, Song ZG, Liew KM. State-space Levy method for vibration analysis of FG-
679 CNT composite plates subjected to in-plane loads based on higher-order shear
680 deformation theory. Compos Struct 2015;134:989–1003.
681 https://doi.org/10.1016/j.compstruct.2015.08.138.
682 [27] Sun Y, Liew KM. The buckling of single-walled carbon nanotubes upon bending: The
683 higher order gradient continuum and mesh-free method. Comput Methods Appl Mech
684 Eng 2008;197:3001–13. https://doi.org/10.1016/j.cma.2008.02.003.
685 [28] Zhang LW, Song ZG, Liew KM. Computation of aerothermoelastic properties and active
686 flutter control of CNT reinforced functionally graded composite panels in supersonic
687 airflow. Comput Methods Appl Mech Eng 2016;300:427–41.
688 https://doi.org/10.1016/j.cma.2015.11.029.
689 [29] Zhang LW, Liew KM. Large deflection analysis of FG-CNT reinforced composite skew
690 plates resting on Pasternak foundations using an element-free approach. Compos Struct
691 2015;132:974–83. https://doi.org/10.1016/j.compstruct.2015.07.017.
692 [30] Sun WK, Zhang LW, Liew KM. A smoothed particle hydrodynamics–peridynamics
693 coupling strategy for modeling fluid–structure interaction problems. Comput Methods
694 Appl Mech Eng 2020;371. https://doi.org/10.1016/j.cma.2020.113298.
695 [31] Abdoh DA, Kodur VKR, Liew KM. Smoothed particle hydrodynamics modeling of the
696 thermal behavior of double skin facades in fires considering the effects of venetian blinds.
697 Appl Math Model 2020;84:357–76. https://doi.org/10.1016/j.apm.2020.02.033.
698 [32] Schnabel D, Özkaya E, Biermann D, Eberhard P. Modeling the motion of the cooling
699 lubricant in drilling processes using the finite volume and the smoothed particle
700 hydrodynamics methods. Comput Methods Appl Mech Eng 2018;329:369–95.
701 https://doi.org/10.1016/j.cma.2017.09.015.
702 [33] Abdoh DA, Ademiloye AS, Liew KM. Modeling glass cooling mechanism with down-
703 flowing water film via the smoothed particle hydrodynamics. Comput Methods Appl
704 Mech Eng 2020;362:112839. https://doi.org/10.1016/j.cma.2020.112839.

[34] Abdoh DA, Ademiloye AS, Liew KM. A meshfree analysis of the thermal behaviors of hot surface glass pane subjects to down-flowing water film via smoothed particle hydrodynamics. Eng Anal Bound Elem 2020;120:195–210. https://doi.org/10.1016/j.enganabound.2020.08.014.

[35] Wawreńczuk A, Kuhnert J, Siedow N. FPM computations of glass cooling with radiation. Comput Methods Appl Mech Eng 2007;196:4656–71. https://doi.org/10.1016/j.cma.2007.05.025.

[36] Samaniego E, Anitescu C, Goswami S, Nguyen-Thanh VM, Guo H, Hamdia K, et al. An energy approach to the solution of partial differential equations in computational mechanics via machine learning: Concepts, implementation and applications. Comput Methods Appl Mech Eng 2020;362:112790. https://doi.org/10.1016/j.cma.2019.112790.

[37] Gu Y, Wang L, Chen W, Zhang C, He X. Application of the meshless generalized finite difference method to inverse heat source problems. Int J Heat Mass Transf 2017;108:721–9. https://doi.org/10.1016/j.ijheatmasstransfer.2016.12.084.

[38] Gavete L, Gavete ML, Benito JJ. Improvements of generalized finite difference method and comparison with other meshless method. Appl Math Model 2003;27:831–47. https://doi.org/10.1016/S0307-904X(03)00091-X.

[39] Kamyabi A, Kermani V, Kamyabi M. Improvements to the meshless generalized finite difference method. Eng Anal Bound Elem 2019;99:233–43. https://doi.org/10.1016/j.enganabound.2018.11.002.

[40] Vu-Bac N, Lahmer T, Zhuang X, Nguyen-Thoi T, Rabczuk T. A software framework for probabilistic sensitivity analysis for computationally expensive models. Adv Eng Softw 2016;100:19–31. https://doi.org/10.1016/j.advengsoft.2016.06.005.

[41] Abdoh DA, Yin BB, Kodur VKR, Liew KM. Computationally efficient and effective peridynamic model for cracks and fractures in homogeneous and heterogeneous materials. Comput Methods Appl Mech Eng 2022;399:115318. https://doi.org/10.1016/j.cma.2022.115318.

[42] Abdoh DA, Yin BB, Liew KM. A phase-field thermomechanical framework for modeling failure and crack evolution in glass panes under fire. Comput Methods Appl Mech Eng 2021;385:114068. https://doi.org/10.1016/j.cma.2021.114068.

[43] Yin BB, Sun WK, Zhang Y, Liew KM. Modeling via peridynamics for large deformation and progressive fracture of hyperelastic materials. Comput Methods Appl Mech Eng 2023;403:115739. https://doi.org/10.1016/j.cma.2022.115739.

[44] Wang Y, Hu J. Performance of laminated glazing under fire conditions. Compos Struct 2019;223:110903. https://doi.org/10.1016/j.compstruct.2019.110903.

[45] Shao G, Wang Q, Zhao H, Wang Y, Sun J, He L. Thermal Breakage of Tempered Glass Façade with Down-Flowing Water Film Under Different Heating Rates. Fire Technol 2016;52:563–80. https://doi.org/10.1007/s10694-015-0499-5.